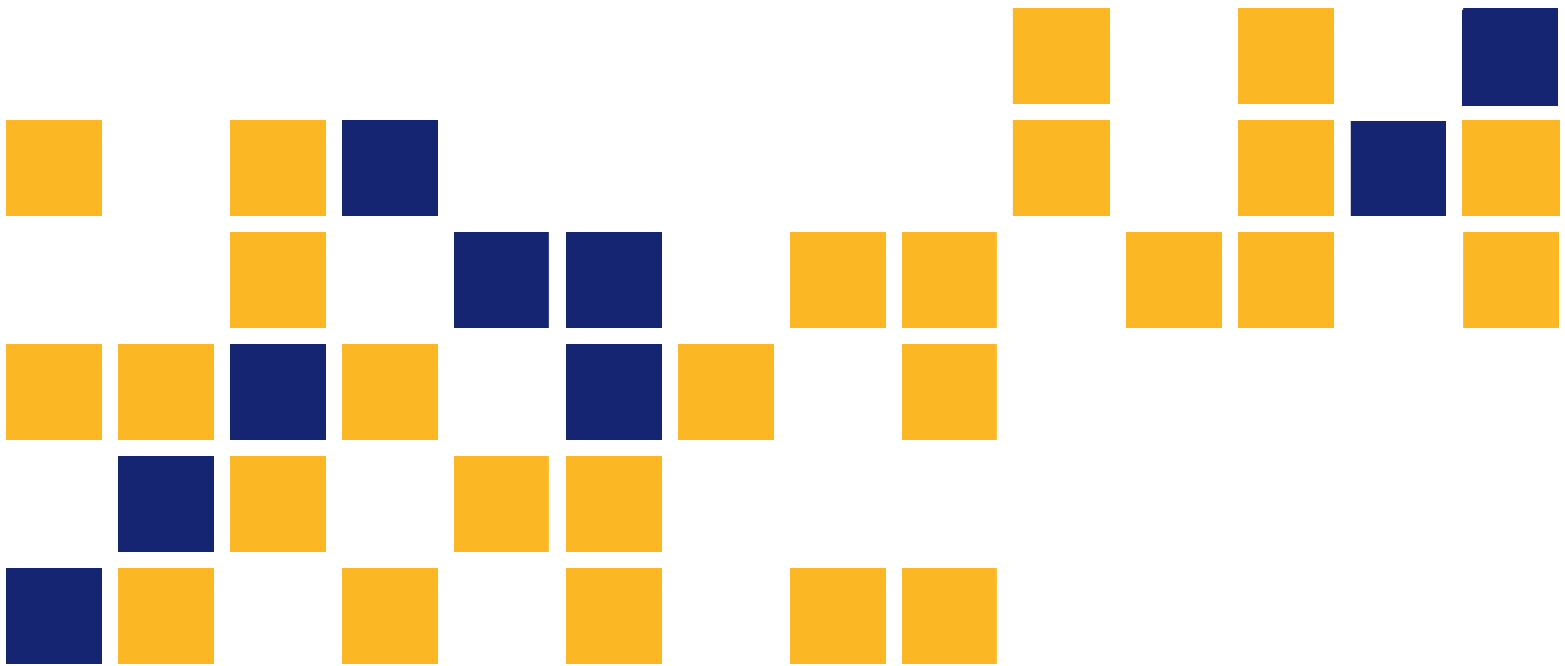# Classification of Wind Farm Turbulence and Its Effects on General Aviation Aircraft and Airports

Zhongquan Charlie Zheng, Ph.D.
Huixuan Wu, Ph.D.

The University of Kansas

Kansas
Department of Transportation

1	Report No.	2	Government Accession No.	3	Recipient Catalog No.	
	K-TRAN: KU-16-3					
4	**Title and Subtitle**			**5**	**Report Date**	
	Classification of Wind Farm Turbulence and Its Effects on General Aviation Aircraft and Airports				January 2018	
				6	**Performing Organization Code**	
7	**Author(s)**			**7**	**Performing Organization Report No.**	
	Zhongquan Charlie Zheng, Ph.D., Huixuan Wu, Ph.D.					
9	**Performing Organization Name and Address**			**10**	**Work Unit No. (TRAIS)**	
	The University of Kansas					
	Department of Aerospace Engineering			**11**	**Contract or Grant No.**	
	1530 West 15th St				C2068	
	Lawrence, Kansas 66045-7609					
12	**Sponsoring Agency Name and Address**			**13**	**Type of Report and Period Covered**	
	Kansas Department of Transportation				Final Report	
	Bureau of Research				October 2015–March 2017	
	2300 SW Van Buren					
	Topeka, Kansas 66611-1195			**14**	**Sponsoring Agency Code**	
					RE-0695-01	
15	**Supplementary Notes**					
	For more information write to address in block 9.					

Wind turbines located on sites known as wind farms have become popular in the United States and elsewhere because they may be able to reduce, if not replace, the use of fossil fuels for energy production. The development of wind farms has been particularly rapid in recent years along the so-called "wind corridors" in such areas as Kansas, Nebraska, Iowa, and South Dakota, thanks to their relatively flat terrain and locations downwind from the Rocky Mountains range. Since February 2013, when there were about 15 existing wind farms and more than 50 wind projects proposed in the state of Kansas, additional proposals have been generated through mid-year 2015. Each proposal typically has several dozen turbines associated with it at the project site. When the proposed sites are in proximity to airports, there is an important question to answer about the impact of turbulence generated by the turbines' rotating blades: is the impact particularly high on General Aviation (GA) aircraft due to their lightweight airframes and their operations typically being at lower altitudes? It is for these reasons that concern exists among general aviation pilots, aerial agricultural applicators, and air ambulance operators, along with airport managers and aviation associations, that the wake turbulence from the spinning blades of wind turbines may create a hazard to aviation/airport safety.

A literature review has revealed that very little research has been conducted to address the concern. In a previous project with the Kansas Department of Transportation (KDOT) completed in 2013 (Mulinazzi & Zheng, 2014), it has been found that the spinning blades from wind turbines can create turbulence, in the form of rotational vortices. It is already known that such vortices can sustain strength and distance for several miles before fully dissipating. Given the results of this previous study, which also formulated a "*hazard index*," consideration should be given during the planning stage of wind farms for the relationship between their locations and any nearby airport, or area of high aircraft use. These considerations also include aerial agricultural applicators and air ambulance providers. It should be noted that the "*hazard index*" is not an industry standard. Rather, it is a term developed by the current authors as a measure to quantify the relative level of hazard.

In this project, studies were performed to draw the proper correlation between the "*hazard index*," developed in a previous study (Mulinazzi & Zheng, 2014), and the safe operation of aircraft at low airspeeds and at low flight altitudes when operating near wind turbine sites or at general aviation airports that are in proximity to wind farms. It is expected that the correlation would help in the planning of future wind farms and siting turbines to prevent detrimental effects for GA operations. Theoretical and applied investigations in this project are used to determine applicability of the "*hazard index*" to a commonly-used GA aircraft and proximity of wind turbines to specific airports. With one type of aircraft as an example, the results can be extended to other GA types of aircraft accordingly.

17	**Key Words**	**18**	**Distribution Statement**		
	Wind Turbine, Wind Farm, Aviation, Airports		No restrictions. This document is available to the public through the National Technical Information Service www.ntis.gov.		
19	**Security Classification (of this report)**	**20**	**Security Classification (of this page)**	**21 No. of pages**	**22 Price**
	Unclassified		Unclassified	45	

Form DOT F 1700.7 (8-72)

This page intentionally left blank.

Classification of Wind Farm Turbulence and Its Effects on General Aviation Aircraft and Airports

Final Report

Prepared by

Zhongquan Charlie Zheng, Ph.D.
Huixuan Wu, Ph.D.

The University of Kansas

PREFACE

The Kansas Department of Transportation's (KDOT) Kansas Transportation Research and New-Developments (K-TRAN) Research Program funded this research project. It is an ongoing, cooperative and comprehensive research program addressing transportation needs of the state of Kansas utilizing academic and research resources from KDOT, Kansas State University and the University of Kansas. Transportation professionals in KDOT and the universities jointly develop the projects included in the research program.

NOTICE

The authors and the state of Kansas do not endorse products or manufacturers. Trade and manufacturers names appear herein solely because they are considered essential to the object of this report.

This information is available in alternative accessible formats. To obtain an alternative format, contact the Office of Public Affairs, Kansas Department of Transportation, 700 SW Harrison, 2nd Floor – West Wing, Topeka, Kansas 66603-3745 or phone (785) 296-3585 (Voice) (TDD).

DISCLAIMER

The contents of this report reflect the views of the authors who are responsible for the facts and accuracy of the data presented herein. The contents do not necessarily reflect the views or the policies of the state of Kansas. This report does not constitute a standard, specification or regulation.

Abstract

Wind turbines located on sites known as wind farms have become popular in the United States and elsewhere because they may be able to reduce, if not replace, the use of fossil fuels for energy production. The development of wind farms has been particularly rapid in recent years along the so-called "wind corridors" in such areas as Kansas, Nebraska, Iowa, and South Dakota, thanks to their relatively flat terrain and locations downwind from the Rocky Mountains range. Since February 2013, when there were about 15 existing wind farms and more than 50 wind projects proposed in the state of Kansas, additional proposals have been generated through mid-year 2015. Each proposal typically has several dozen turbines associated with it at the project site. When the proposed sites are in proximity to airports, there is an important question to answer about the impact of turbulence generated by the turbines' rotating blades: is the impact particularly high on General Aviation (GA) aircraft due to their lightweight airframes and their operations typically being at lower altitudes? It is for these reasons that concern exists among general aviation pilots, aerial agricultural applicators, and air ambulance operators, along with airport managers and aviation associations, that the wake turbulence from the spinning blades of wind turbines may create a hazard to aviation/airport safety.

A literature review has revealed that very little research has been conducted to address the concern. In a previous project with the Kansas Department of Transportation (KDOT) completed in 2013 (Mulinazzi & Zheng, 2014), it has been found that the spinning blades from wind turbines can create turbulence, in the form of rotational vortices. It is already known that such vortices can sustain strength and distance for several miles before fully dissipating. Given the results of this previous study, which also formulated a "*hazard index*," consideration should be given during the planning stage of wind farms for the relationship between their locations and any nearby airport, or area of high aircraft use. These considerations also include aerial agricultural applicators and air ambulance providers. It should be noted that the "*hazard index*" is not an industry standard. Rather, it is a term developed by the current authors as a measure to quantify the relative level of hazard.

In this project, studies were performed to draw the proper correlation between the "*hazard index*," developed in a previous study (Mulinazzi & Zheng, 2014), and the safe operation of aircraft at low airspeeds and at low flight altitudes when operating near wind turbine sites or at general aviation airports that are in proximity to wind farms. It is expected that the correlation would help in the planning of future wind farms and siting turbines to prevent detrimental effects for GA operations. Theoretical and applied investigations in this project are used to determine applicability of the "*hazard index*" to a commonly-used GA aircraft and proximity of wind turbines to specific airports. With one type of aircraft as an example, the results can be extended to other GA types of aircraft accordingly.

Table of Contents

List of Tables

List of Figures

Chapter 1: Introduction

Wind turbines located on sites known as wind farms have become popular in the United States and elsewhere because they may be able to reduce, if not replace, the use of fossil fuels for energy production. The development of wind farms has been particularly rapid in recent years along the so-called "wind corridors" in such areas as Kansas, Nebraska, Iowa, and South Dakota, thanks to their relatively flat terrain and locations downwind from the Rocky Mountains range. Since February 2013, when there were about 15 existing wind farms and more than 50 wind projects proposed in the state of Kansas, additional proposals have been generated through mid-year 2015. Each proposal typically has several dozen turbines associated with it at the project site. When the proposed sites are in proximity to airports, there is an important question to answer about the impact of turbulence generated by the turbines' rotating blades: is the impact particularly high on General Aviation (GA) aircraft due to their lightweight airframes and their operations typically being at lower altitudes? It is for these reasons that concern exists among general aviation pilots, aerial agricultural applicators, and air ambulance operators, along with airport managers and aviation associations, that the wake turbulence from the spinning blades of wind turbines may create a hazard to aviation/airport safety.

A literature review has revealed that very little research has been conducted to address the concern. In a previous project with the Kansas Department of Transportation (KDOT) completed in 2013 (Mulinazzi & Zheng, 2014), it has been found that the spinning blades from wind turbines can create turbulence, in the form of rotational vortices. It is already known that such vortices can sustain strength and distance for several miles before fully dissipating. Given the results of this previous study, which also formulated a "*hazard index*," consideration should be given during the planning stage of wind farms for the relationship between their locations and any nearby airport, or area of high aircraft use. These considerations also include aerial agricultural applicators and air ambulance providers. It should be noted that the "*hazard index*" is not an industry standard. Rather, it is a term developed by the current authors as a measure to quantify the relative level of hazard.

In this project, studies were performed to draw the proper correlation between the "*hazard index*," developed in a previous study (Mulinazzi & Zheng, 2014), and the safe operation of aircraft at low airspeeds and at low flight altitudes when operating near wind turbine sites or at general aviation airports that are in proximity to wind farms. It is expected that the correlation would help in the planning of future wind farms and siting turbines to prevent detrimental effects for GA operations. Theoretical and applied investigations in this project are used to determine applicability of the "*hazard index*" to a commonly-used GA aircraft and proximity of wind turbines to specific airports. With one type of aircraft as an example, the results can be extended to other GA types of aircraft accordingly.

Chapter 2: Theoretical Models

2.1 Helical Vortex Model

Wind turbine wakes are modeled by helical vortices. Figure 2.1 (Fukumoto & Okulov, 2005) shows the coordinate system and the center line of a helical vortex:
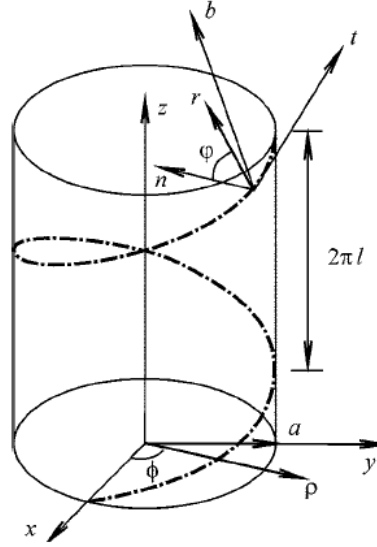
Figure 2.1: Coordinate system and the center line of a helical vortex

In a cylindrical coordinate system, the velocity field is described as follows:

$$u_\rho = \frac{\Gamma}{2\pi\rho l} \sqrt[4]{(l^2 + \rho^2)(l^2 + a^2)} Im \left\{ \frac{e^{i\chi}}{e^{\mp\xi} - e^{i\chi}} \right.$$

$$\pm \frac{l}{24} \left[\frac{2l^2 + 9a^2}{(l^2 + a^2)^{3/2}} - \frac{2l^2 + 9\rho^2}{(l^2 + \rho^2)^{3/2}} \right] log(1 - e^{\pm\xi + i\chi}) \right\},$$

$$u_z = \frac{\Gamma}{2\pi l} \left\{ \begin{matrix} 1 \\ 0 \end{matrix} \right\} + \frac{\Gamma}{2\pi l} \frac{\sqrt[4]{(l^2 + a^2)}}{\sqrt[4]{(l^2 + \rho^2)}} Re \left\{ \frac{\pm e^{i\chi}}{e^{\mp\xi} - e^{i\chi}} \right.$$

$$+ \frac{l}{24} \left[\frac{3\rho^2 - 2l^2}{(l^2 + \rho^2)^{3/2}} + \frac{2l^2 + 9a^2}{(l^2 + a^2)^{3/2}} \right] log(1 - e^{\xi + i\chi}) \right\},$$

$$u_\phi = \frac{\Gamma}{2\pi l} - \frac{l u_z}{\rho}$$

Equation 2.1

Where Γ is the circulation of the vortex filament, a is the radius of the helical vortex, $2\pi l$ is the pitch and $\chi = \phi - z/l$. Here the top line in braces corresponds for $\rho < a$, the bottom one to that $\rho > a$.

In a helical vortex model (Hardin, 1982) used in the previous study (Mulinazzi & Zheng, 2014), there was a singularity at the center of the helical vortex model which resulted in over-estimated velocity values in the airflow close to the vortex center. To avoid the singularity at the center of the helical vortex filament, the velocity inside the tube is modeled as a rotation core in this model (Fukumoto & Okulov, 2005):

$$v = \frac{\Gamma}{2\pi\sigma^2}r, \qquad (r \leq \sigma) \hspace{3cm} \textbf{Equation 2.2}$$

Where σ is the core size of the helical vortex and selected here as 5% of the turbine diameter.

The helical vortex circulation is needed for the model. Since it is difficult to get data of a vortex generated by a real-size wind turbine, we calculate the circulation based on the measurement in Sherry, Sheridan, and Lo Jacono (2013). The experimental study in Sherry et al. tested non-dimensionalized maximum blade-bound circulation under different tip speed ratios. The maximum value of the circulation of a full-scale wind turbine is 0.143:

$$\frac{\Gamma_m}{U_\infty R} = 0.143 \hspace{3cm} \textbf{Equation 2.3}$$

Where R is the radius of the wind turbine, 91.44 m in the wind farm case studied here, U_∞ is the inflow velocity, which equals to 40 mph (17.88 m/s) the maximum wind speed considered in the wind farm case. We thus can calculate the circulation of the vortex of the real-size wind turbine considered in this study, which is 116.89 m^2/s.

2.2 Induced Rolling Moment Coefficient on the Aircraft that Encounter the Wake

Since we have the wind turbine wake velocity field from the helical vortex model, we can calculate the induced rolling moment coefficient on an airplane that flies through the wake (Zheng & Xu, 2008). Considering the aircraft with a wing span of $2s_F$ and flying speed W_F, we have, for the lift force acting on a spanwise element section dx_F:

$$\rho W_F \Gamma_F(x_F) dx_F = \frac{1}{2} \rho W_F{}^2 C_{LF}(x_F) \, dx_F \cdot c_F(x_F)$$

<div align="right">**Equation 2.4**</div>

Where Γ_F is the circulation of the aircraft wing at x_F, C_{LF} is the lift coefficient, and $c_F(x_F)$ is the chord length of the aircraft at x_F. Assuming that $\partial C_{LF}/\partial\alpha$ is approximately constant in the range of angle of attack α, we have:

$$\Gamma_F(x_F) = \frac{1}{2} W_F \Delta\alpha \frac{\partial C_{LF}}{\partial\alpha} \cdot c_F(x_F)$$

<div align="right">**Equation 2.5**</div>

Since:

$$\Delta\alpha \approx \frac{v}{W_F}$$

<div align="right">**Equation 2.6**</div>

Where v is the vertical velocity component at the location of the wing (produced by the wake vortex system), we have:

$$\Gamma_F(x_F) = \frac{1}{2} v(x_F) \frac{\partial C_{LF}}{\partial\alpha} c_F(x_F)$$

<div align="right">**Equation 2.7**</div>

The rolling moment on the wing can then be expressed by:

$$M_{RF} = \int_{-S_F}^{S_F} \rho W_F \Gamma_F(x_F) x_F dx_F = \frac{1}{2} \rho W_F \frac{\partial C_{LF}}{\partial\alpha} \int_{-S_F}^{S_F} v(x_F) c_F(x_F) \, x_F dx_F$$

<div align="right">**Equation 2.8**</div>

And the rolling moment coefficient is:

$$C_{RF} = \frac{M_{RF}}{\frac{1}{2} \rho W_F{}^2 S_F \cdot 2s_F} = \frac{\partial C_{LF}}{\partial\alpha} \cdot \frac{1}{W_F S_F \cdot 2s_F} \int_{-S_F}^{S_F} v(x_F) c_F(x_F) x_F dx_F$$

<div align="right">**Equation 2.9**</div>

Where S_F is the plan form area and is defined as:

$$S_F = 2s_F \bar{c}_F$$

<div align="right">**Equation 2.10**</div>

With $\bar{c}_F$ equal to the average chord length of the wing.

The airplane considered here is a Cessna 172. The airfoil used is NACA2412, for which the value of $\frac{\partial C_{LF}}{\partial \alpha}$ is approximately equal to 5.73 /rad. In addition, $\bar{c}_F$ is the average chord length, and W_F is the flying speed. For the cases studied here, the flying speed of the airplane is selected to be 60 knots (30.86 m/s; Goode, O'Bryan, Yenni, Cannaday, & Mayo, 1976), which is a typical flying speed of a GA-type airplane during take-off or landing, as we are mostly interested in aircraft during take-off or landing near airports. The chord length changes along the spanwise direction and approximately follows:

$$\frac{c_F(x_F)}{\bar{c}_F} = \frac{20}{13}(1 - 0.7\,|\frac{x_F}{s_F}|) \qquad \text{Equation 2.11}$$

The rolling moment coefficient that the airplane is able to operate is modeled by:

$$C_R = C_{l\delta_A}\delta_A \qquad \text{Equation 2.12}$$

Where δ_A is the aileron angle of the airplane. For a Cessna 172, the aileron coefficient, $C_{l\delta_A}$, is 0.178 (Roskam, 1979).

The range of the operable aileron angle can be found in Sadraey (2012) as:

$$0 < \delta_A < 14° \text{ (or 0.244 rad)} \qquad \text{Equation 2.13}$$

Therefore, at the maximum operable aileron angle, the maximum sustainable rolling moment coefficient is $C_R = 0.0435$.

2.3 Wake Vortex Decay Model

The instantaneous wake vortex circulation, Γ_i, can be calculated based on the initial wake circulation, Γ_0, and vortex span b_0 after time t (Zheng, Xu, & Wilson, 2009). Here, we assume that the wind turbine wake vortex decays in a similar way as the aircraft wake vortex. The decay law follows those developed by Sarpkaya, Robins, and Delisi (2001).

$$\frac{\Gamma_i}{\Gamma_0} = \exp(-C\,\frac{t\Gamma_0}{2\pi b_0{}^2 T_c{}^*}) \qquad \text{Equation 2.14}$$

Where C is a constant of 0.45, and $T_c{}^*$ is determined by the following calculation:

$$\varepsilon^* = \frac{2\pi b_0}{\Gamma_0}(\varepsilon b_0)^{1/3}$$

Equation 2.15

For a high turbulence case at the turbulent intensity 10%, ε is $0.01\ m^2/s^3$ in this case, which indicates that ε^* has a high value and the eddy-dissipation rate can be approximately calculated as (Zheng et al., 2009):

$$\varepsilon^*(T_c^*)^{4/3} = 0.7475$$

Equation 2.16

So,

$$T_c^* = (\frac{0.7475}{\varepsilon^*})^{3/4} = (\frac{0.7475\Gamma_0}{2\pi b_0(\varepsilon b_0)^{1/3}})^{3/4}$$

Equation 2.17

$$\frac{\Gamma_i}{\Gamma_0} = \exp\left(-C\frac{t\Gamma_0}{2\pi b_0{}^2\left(\dfrac{0.7475\Gamma_0}{2\pi b_0(\varepsilon b_0)^{\frac{1}{3}}}\right)^{\frac{3}{4}}}\right) = \exp\left(\frac{-Ct(\varepsilon\Gamma_0)^{1/4}}{0.956(\pi)^{1/4}b_0}\right)$$

Equation 2.18

At a distance S with the wind speed V_0,

$$t = \frac{S}{V_0}$$

Equation 2.19

$$\frac{\Gamma_i}{\Gamma_0} = \exp\left(\frac{-CS(\varepsilon\Gamma_0)^{0.25}}{1.2727V_0 b_0}\right)$$

Equation 2.20

In the next section, this decay model is compared with the Navier–Stokes simulation using the actuator-line method to represent the wind turbine blades, and a good agreement has been achieved.

2.4 Actuator-Line Method for Wind Turbine Wake Simulation

The actuator-line method bridges the difference in model details and accuracy between the direct rotor simulations and the less-complete actuator disk models (O'Dea & Guessous, 2016). The actuator-line method and the immersed-boundary methods (Zhang & Zheng, 2007) are similar. They both create a forcing term into the flow without really putting the object in the flow field. The difference is that there is no geometry of the object in the fluid in the actuator-line method. Instead of simulating the real geometry of the wind turbine blades, the blades are modeled as rotating actuator lines in place of the physical blades. This provides force into the flow field. The force is distributed to the grid point using Gaussian function (Troldborg, 2009; Peet, Fischer, Conzelmann, & Kotamarthi, 2013; Jin, 2013). The actuator-line method and the Gaussian distribution used in this study are from Troldborg (2009) and Peet et al. (2013).

In the case of wind turbine induced helical vortex simulation, a 3D actuator-line method implementation in O'Dea and Guessous (2016) is selected. In this method, there is no physical boundary in the simulation domain. Instead, an actuator line model is built and the lift and drag force are calculated based on the airfoil data and the angle-of-attack (AOA) computed in the simulated flow field. This force is applied into the fluids accordingly.
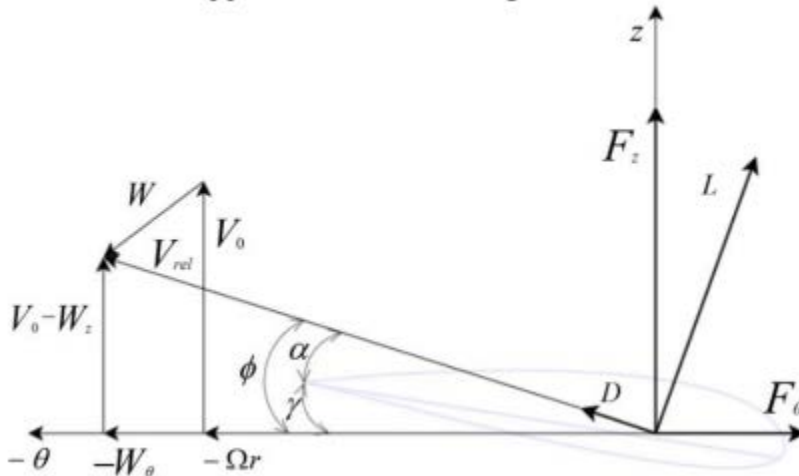
Figure 2.2: Turbine blade forces

In Figure 2.2, the forces are decomposed into the axial and circumferential directions for each section of the turbine blade. The overall relative velocity is defined as:

$$V_{rel}^2 = (V_0 - W_z)^2 + (\Omega r - W_\theta)^2 \hspace{3cm} \textbf{Equation 2.21}$$

Where Ω is the angular velocity, V_0 is the incoming wind velocity, W_z and W_θ are the flow axial velocity and tangential velocity respectively, and r is the radius of the blade section. Then the lift and drag forces are calculated as:

$$\begin{aligned} \boldsymbol{L} &= 0.5\rho V_{rel}^2 cC_l dr\boldsymbol{e_l} \\ \boldsymbol{D} &= 0.5\rho V_{rel}^2 cC_d dr\boldsymbol{e_d} \end{aligned} \hspace{2.5cm} \textbf{Equation 2.22}$$

Where $\boldsymbol{e_l}$ and $\boldsymbol{e_d}$ are the unit vectors for the directions of lift and drag. Coefficients of lift and drag, C_l and C_d, are calculated from curve fitting of the existing wind turbine data. $\alpha = \phi - \gamma$ is the local angle of attack. And γ is the pitching angle from the wind turbine data. The relative motion angle is given by:

$$\phi = tan^{-1}(\frac{V_0 - W_z}{\Omega r - W_\theta}) \hspace{2.8cm} \textbf{Equation 2.23}$$

The force is distributed to nearby computation point using a Gaussian function:

$$\boldsymbol{f}_{line} = (\boldsymbol{L} + \boldsymbol{D})\frac{e^{-d^2/\epsilon^2}}{\epsilon^3\sqrt{\pi}^3} \hspace{2.8cm} \textbf{Equation 2.24}$$

This forcing term is considered feedback forcing from the blade to the fluid in the incompressible Navier–Stokes equations:

$$\begin{aligned} \nabla \cdot \boldsymbol{u} &= 0 \\ \frac{\partial \boldsymbol{u}}{\partial t} &= -(\boldsymbol{u} \cdot \nabla)\boldsymbol{u} + \frac{\nabla p}{\rho} + \mu\nabla^2\boldsymbol{u} - \boldsymbol{f}_{line} \end{aligned} \hspace{1.5cm} \textbf{Equation 2.25}$$

Figure 2.3 shows the iso-surface of vorticity magnitude in the flow field, and Figure 2.4 shows the y-direction vorticity at the Y center cutting plane. Figure 2.5 is the decay of the tip vortex circulation along the wind direction, the x-direction. The red line is their fitted curve and the green line is the decay model from Equation 2.3. It shows that the modeled decay rate predicted from Equation 2.3 agrees with the CFD simulation very well.
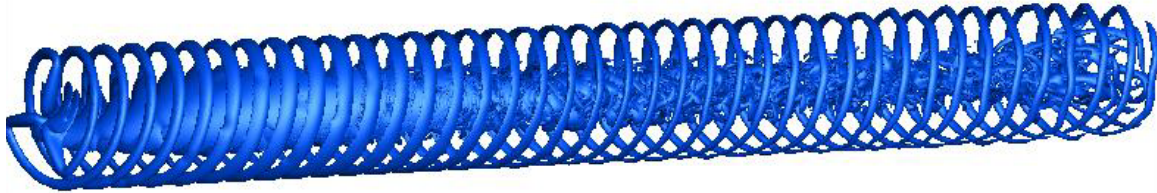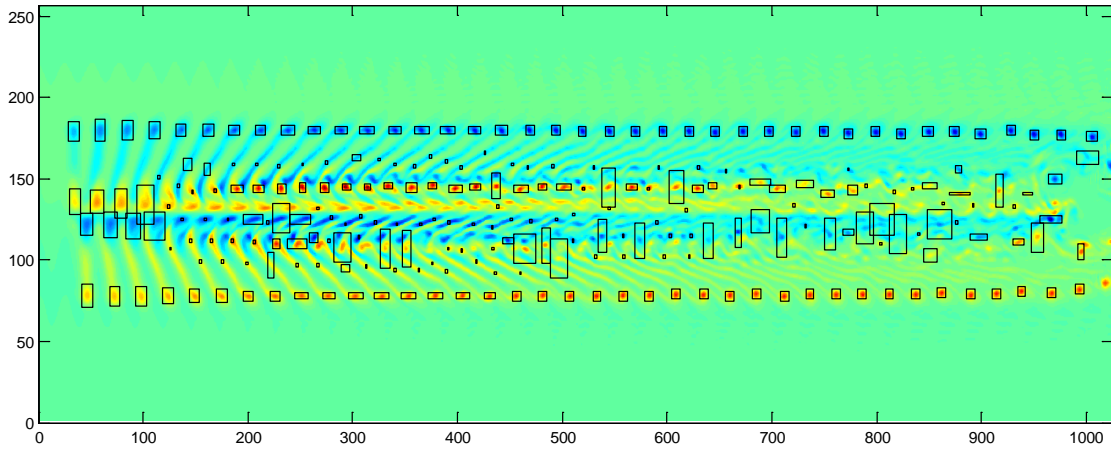
Figure 2.3: ISO surface of vorticity

Figure 2.4: Y-Vorticity at center cutting plane of Y Direction
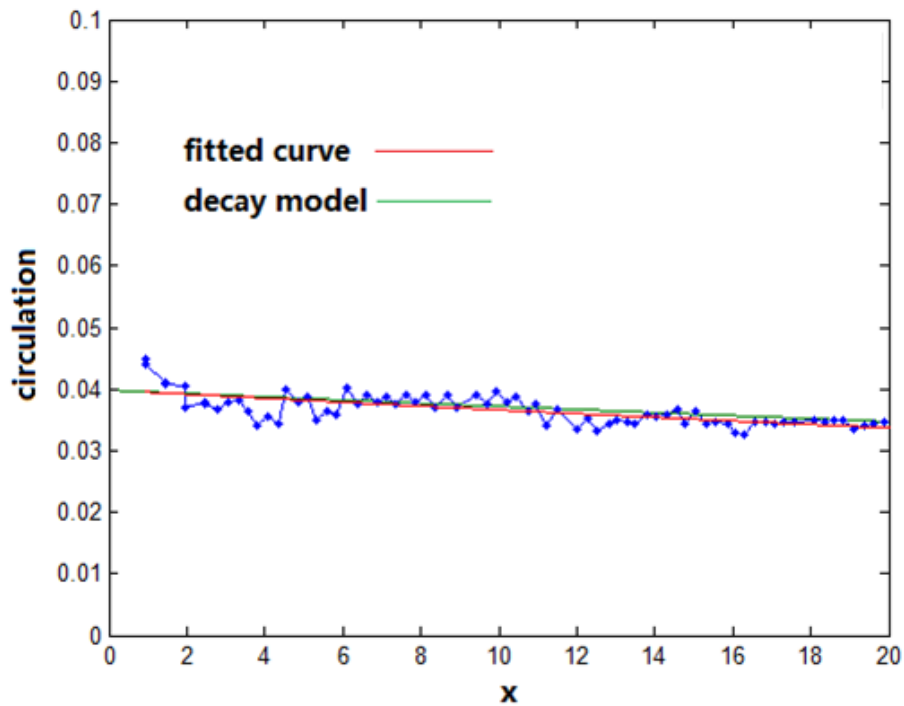

**Figure 2.5: Distribution of circulations and their fitted curve compare well with the decay model**

Chapter 3: Experiment Study

From December 2015 to January 2017, we conducted a series of experimental studies on the wind turbine wakes in the Fluid Dynamics and Applied Optics Laboratory at the University of Kansas. The purpose was to find out the velocity profile, turbulence intensity, variation of velocity deficit, and evolution of vortical structures downstream from a turbine model in controlled aerodynamics conditions. These results could be used as support or guidance for numerical modeling. The experiments included two parts: wind tunnel testing and water tunnel testing. In the wind tunnel, the focus was on profiling and the main tool was thermal anemometry; in the water tunnel, we investigated the evolution of vortex structures using a state-of-the-art optical method called particle image velocimetry.

3.1 Wind Tunnel Tests

3.1.1 Flow Visualization

Flow visualization was performed using smoke and high-speed imaging in the small low-speed wind tunnel (see Figure 3.1). The smoke was sucked into the open-loop tunnel. The pattern of smoke clearly shows the helical shape tip vortex and the complex hub wake.
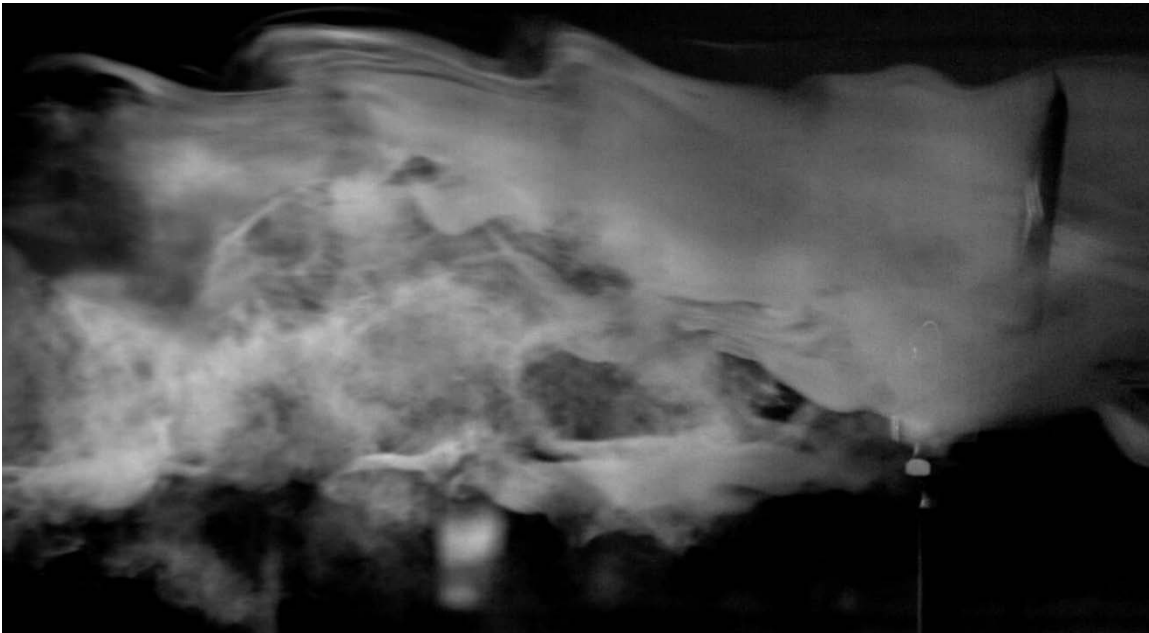
Figure 3.1: Smoke-based flow visualization of the near wake downstream the turbine model. The flow direction is from right to the left. The wavy pattern clearly indicates the location of helical vortex.
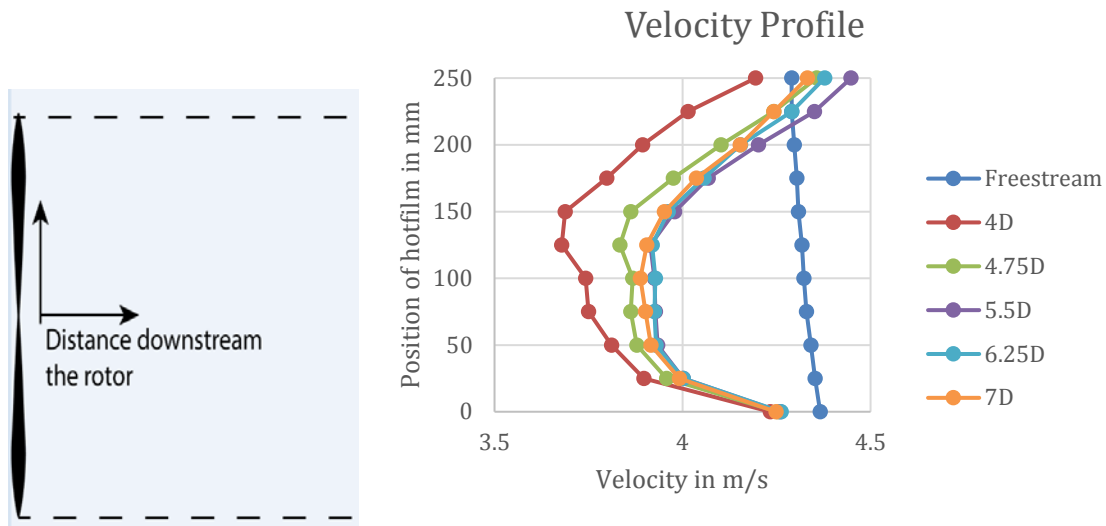
3.1.2 Velocity Profiling

The experiments were conducted in the big low speed wind tunnel. The tunnel cross section is 51 inches by 36 inches. The setup is shown in the following figures. A 9-inch turbine model is placed in the test section; downstream of it is a hotfilm anemometer. The hotfilm is mounted in a motorized translation system that can travel in the stream-wise (Slider 1) and vertical directions (Slider 2). The travel range of Slider 1 is 800 mm and Slider 2 is 250 mm. The distance between the anemometer and turbine model in the measurement is from 4D to 7D. D is the turbine diameter. The incoming flow velocity is 4.3 m/s (5% of the total wind tunnel power), and the turbulent level, *u'/U*, is 0.8%.

Figure 3.2: The experimental setup of the wind tunnel test. Left is the front view and right is the side view.

Five downstream locations are selected: 4D, 4.75D, 5.5D, 6.25D, and 7D. At each of these locations, the hotfilm scans 11 points in the vertical direction to obtain the velocity profile. The following figure shows the measured absolute velocity.

Figure 3.3: The velocity profile at different downstream locations from 4D to 7D. The turbine axis is located at 125 mm in the vertical direction.

The following figure displays the same velocity data in the form of a color map. The recovery of wake center velocity over a long distance is clearly seen.
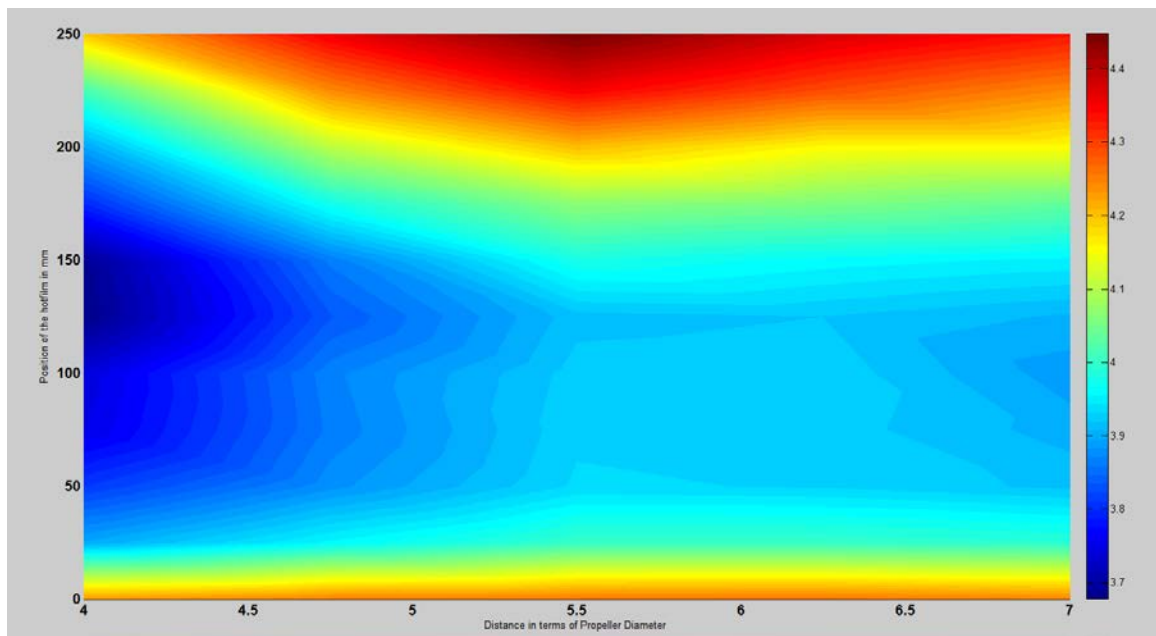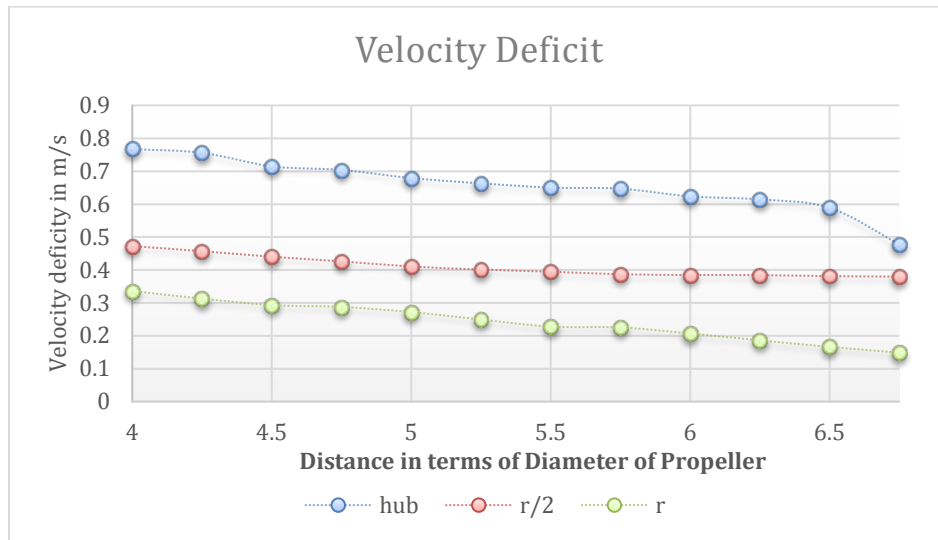

Figure 3.4: Absolute velocity in the turbine wake (from 4D to 7D)

The velocity increases and velocity deficit decreases along the stream direction. The increment at the hub is larger than that at half blade span (r/2) and tip (r), which is shown below.
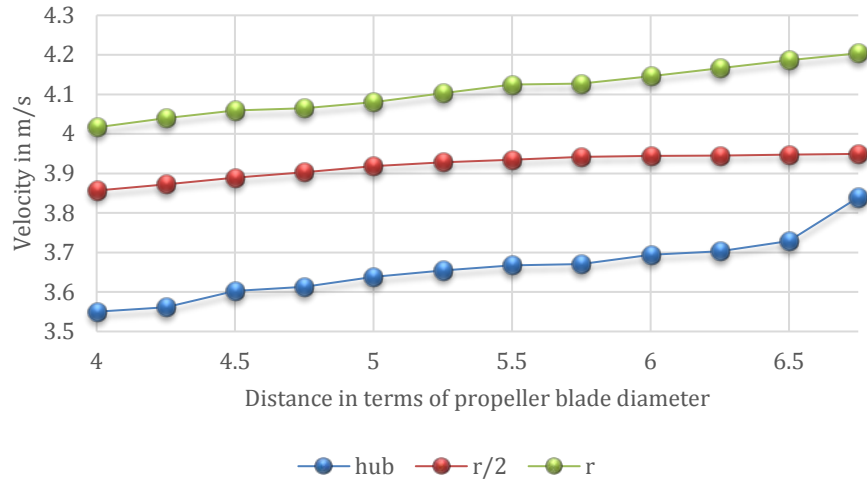
Figure 3.5: Velocity variation in the streamwise direction

Figure 3.6: Velocity deficit variation in the streamwise direction

3.1.3 Power Law Fitting of the Velocity Variation

In the studied area, the velocity deficit at hub, half-span, and tip follows power law decay rate. At the hub, it can be represented by $V_{Def} = 1.577d^{-0.519}$, half span $V_{Def} = 0.890d^{-0.486}$, and tip $V_{Def} = 2.245d^{-1.347}$, where d is the downstream distance normalized by rotor diameter D. They are shown in the following figures.
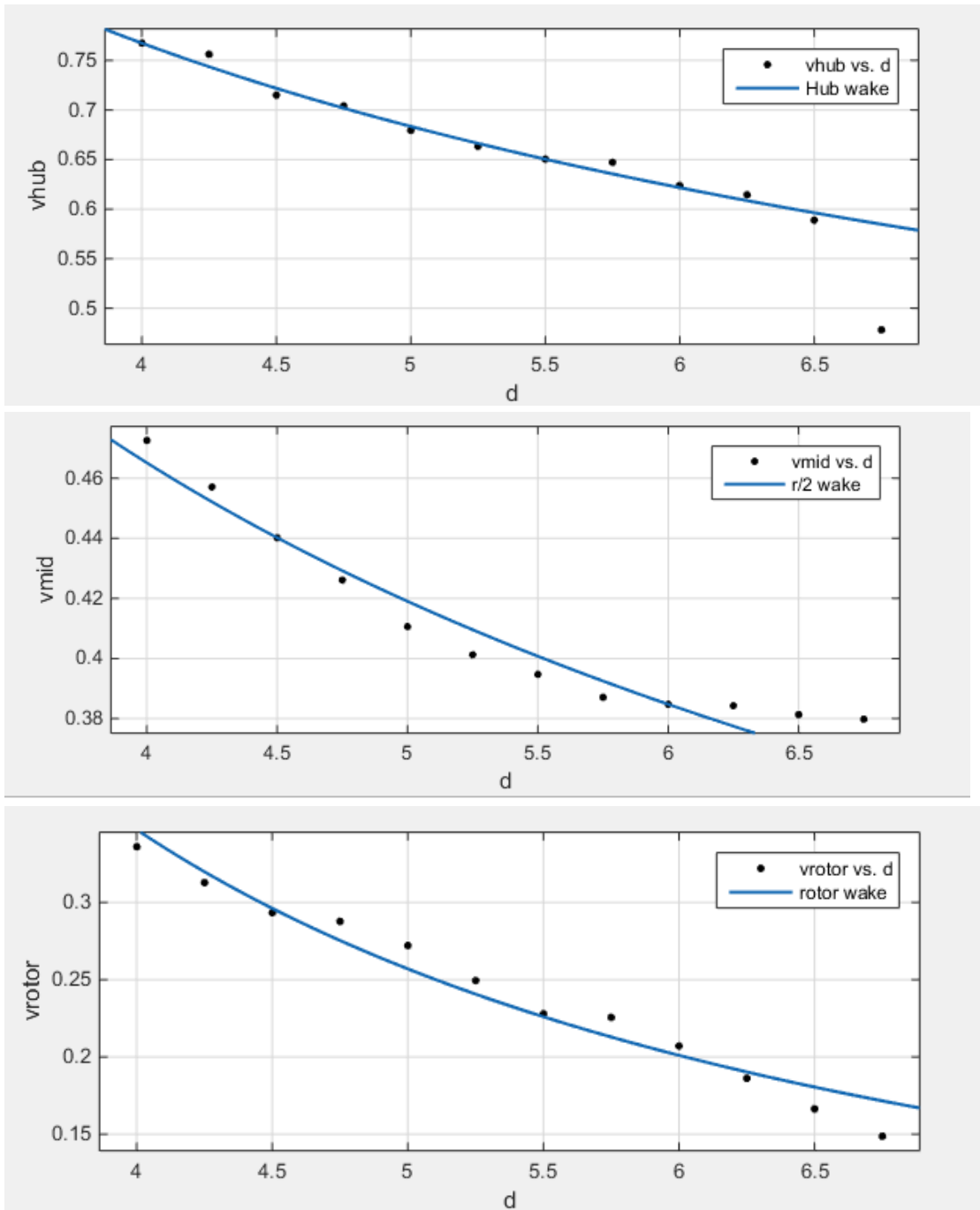
14

Figure 3.7: Power law fitting of the velocity deficit variation in the downstream direction

3.1.4 Turbulence Evolution

Turbulence intensity at the hub decreases; meanwhile, at half-span and the tip, there is a slight increase because there is additional production due to the strong shear. The power law fitting is hub $0.05126\ d^{-0.5833}$, half span $0.00610d^{0.1862}$, and tip $0.01219d^{0.04519}$.
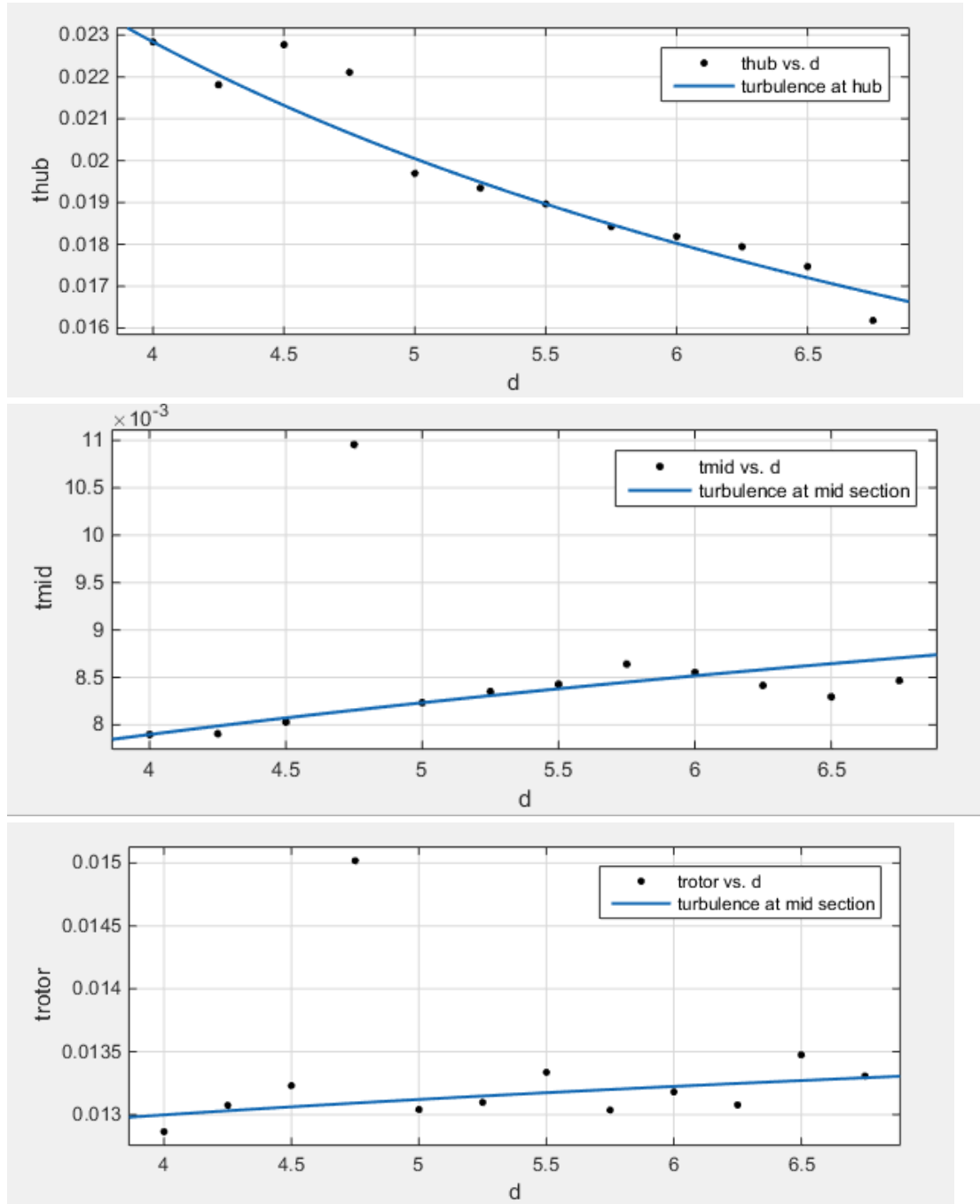

Figure 3.8: The variation of streamwise Reynolds Stress <uu> from 4D to 7D

3.1.5 Calibration of the Hotfilm Anemometer

The hardware of the hotfilm system had small problems due to a loose resistor. After the repair, we conducted calibration and analyzed the spectrum. The following figure shows the calibration curve, i.e., the velocity-voltage reading relation. The numerical equation is:

$$\text{Velocity} = -4.411 V^5 + 59.21\ V^4 - 309.5\ V^3 + 796.1\ V^2 - 1007\ V + 499.1$$
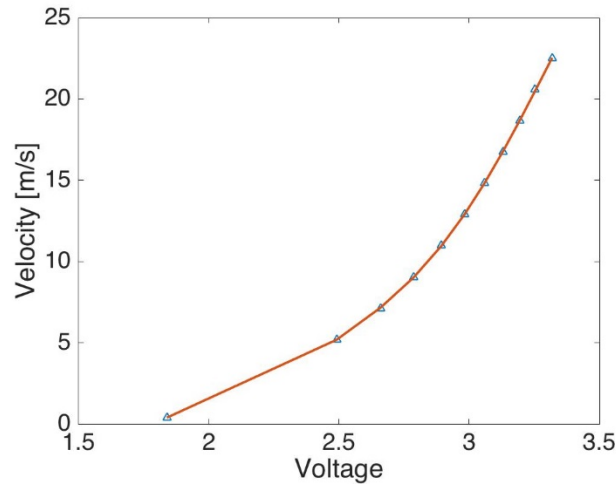
Figure 3.9: Calibrated fitting of the hotfilm. The curved line is a 5th order polynomial and the symbols are experimental measurement data.

The power spectrum density of the voltage signal is shown in the following figure. This test demonstrates that the hotfilm is able to detect signals in the order of 100 Hz, but the noise level at high frequencies is large.
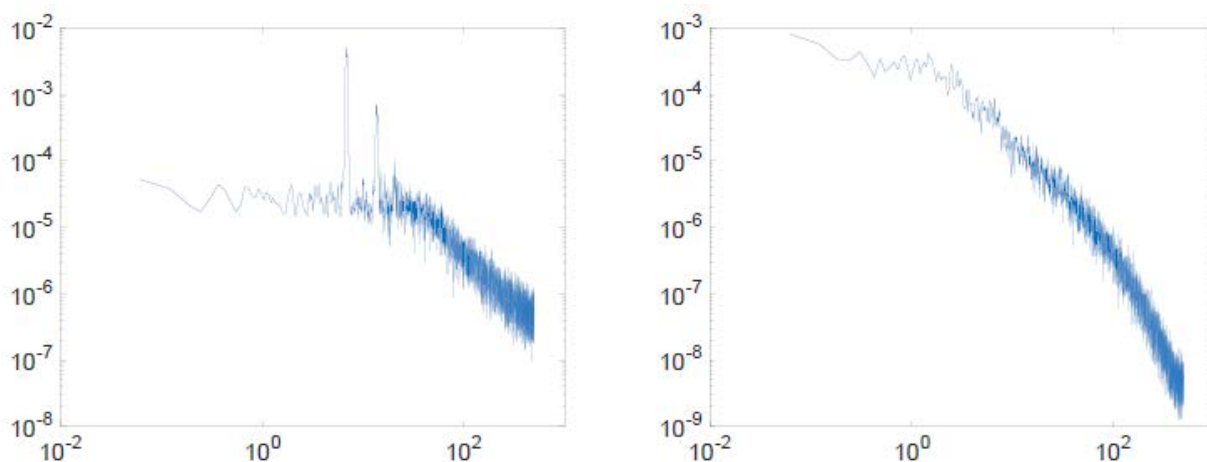

Figure 3.10: Left is the power spectrum density behind a turbine model and right is the spectrum of a free decaying turbulent flow.

3.2 Water Tunnel Tests

3.2.1 Particle Image Velocimetry System

Particle image velocimetry (PIV) system is an optical based flow velocity measurement technology. The principle is to use cameras to record the motion of tracer particles in a complex flow and deduce the velocity by examining the particle displacement in a given time. Our PIV setting is shown in the following figure. The camera is located on the side of our water tunnel. An illumination laser sheet is projected into the field of view in the test section from the bottom. We selected three downstream sections, centered at 1D, 4.25 D, and 9 D, where D is the model diameter (= 5 inch). The wake evolves in the streamwise direction. At 1D downstream the turbine, the velocity deficit and turbulent kinetic energy are large. These quantities decrease along the flow direction. As a result, at 4.25D they are smaller and at 9D they diminish.
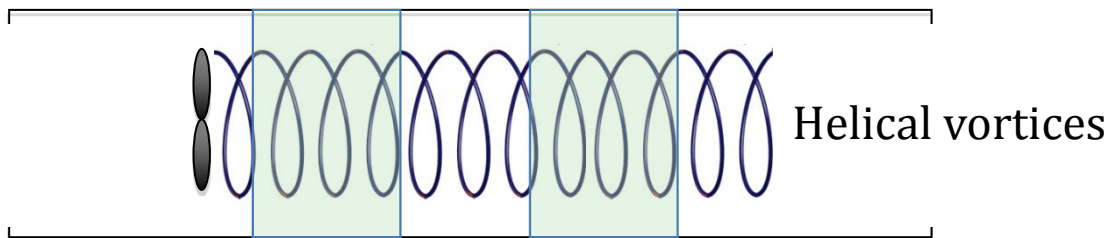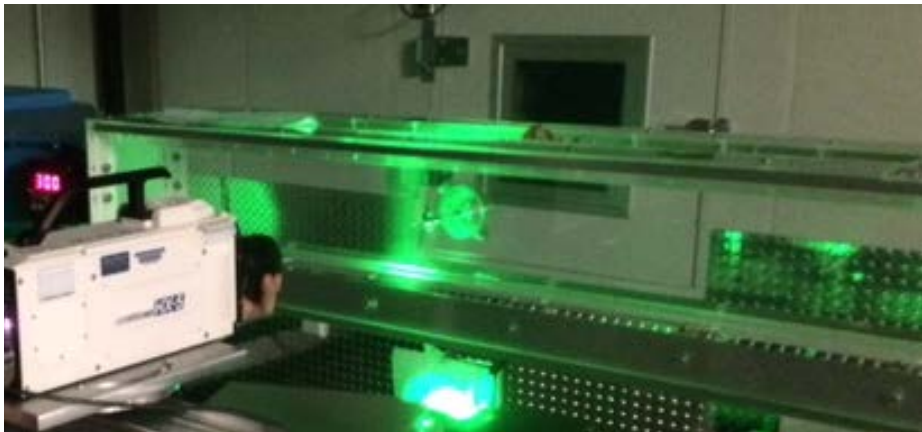
Figure 3.11: Experimental setup. Similar to the wind tunnel experiments, we were interested in the wake flow. The PIV measurements were performed at several locations centered at 1D, 4.25D, and 9D.

3.2.2 Velocity and Turbulence Profiles

We measured velocity profile, wake deficit, turbulent kinetic energy, and energy spectrum. The following figure shows the velocity profile cross the entire turbine diameter. Upstream the turbine, the flow is uniform except for a small disturbance located at r/D = 0.35. The average velocity is 0.58 m/s. At 1D downstream the turbine model, the velocity profile (red line) shows a V-shape. The maximum velocity deficit is located at the hub. Its value is 0.30 m/s. At 4.25D downstream (yellow line), the velocity has recovered. The deficit is 0.14 m/s. At 9D (purple line), the speed at the hub area is nearly recovered, with a deficit 0.05 m/s. The wake velocities at r/D > 0.3 and < –0.3 are bigger than the upstream velocity, partially caused by the boundary effect and partially due to the induced motion of tip vortices.
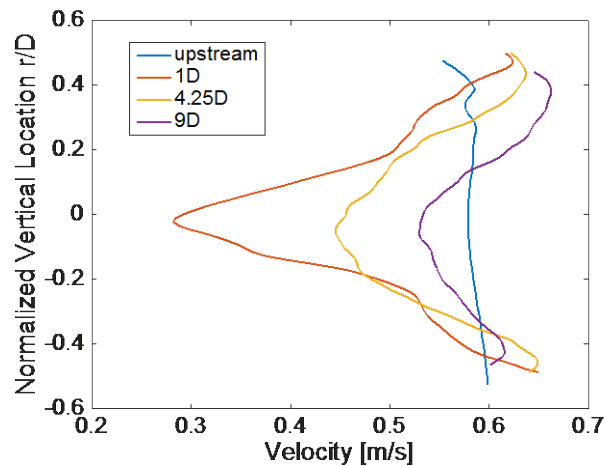
Figure 3.12: Velocity profile of the turbine wake

The recovery of wake velocity follows a power law. The following picture describes the relation between velocity deficit and downstream distance. This relation can be fitted by $\Delta V \sim d^{-0.75}$, where $d = x/D$, the downstream distance normalized by rotor diameter. The theoretical analysis indicates that the velocity deficit ought to decrease following $d^{-0.66}$, but in our setting, the finite cross section of the water tunnel may have increased the velocity recovery.
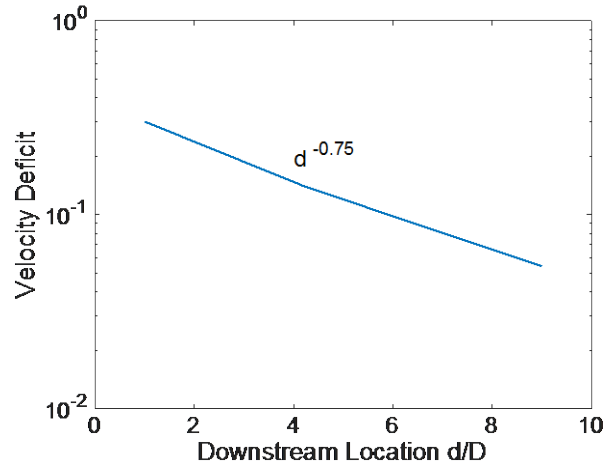
Figure 3.13: The variation of velocity deficit in the streamwise direction

The major concern in our research is the development of turbulence downstream from a turbine. The next figure plots the turbulent kinetic energy profile. This energy is defined as $k=\frac{1}{2}(R_{xx}+R_{yy}+R_{zz})$. The z component is not available from the 2D PIV data, but it is reasonable to assume y and z component are symmetric in the test section, except the vicinity of wall boundaries. So, we use a pseudo number $k=\frac{1}{2}(R_{xx}+R_{yy}+R_{yy})$. Upstream from the model, turbulence is very weak (The disturbance at r/D = 0.3 can be fixed in the future experiments). At 1D downstream, turbulence profile has two peaks, corresponding to the shear layers developed at the hub. They decay quickly. Till 4.25D, the hub-induced turbulence is barely visible at r/D= –0.3. We believe that this is caused by the meandering of hub-vortex, however, we need more experimental evidence to prove it, as the meandering due to vortex induction is difficult to quantify. At 9D, the turbulent energy peaks disappear completely.
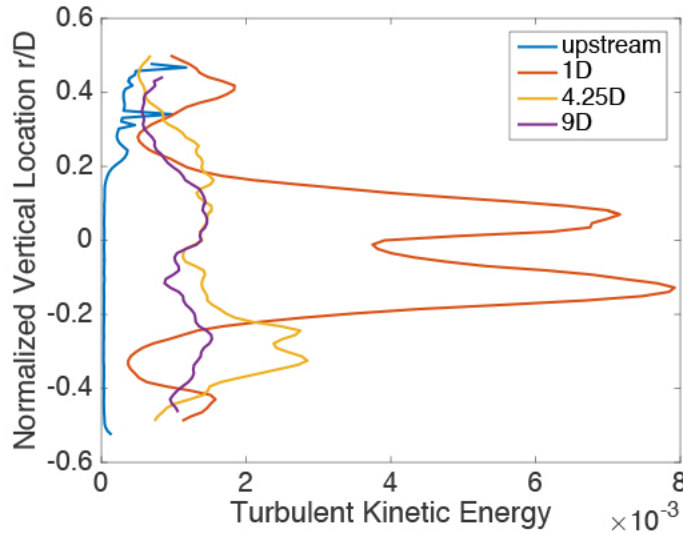
Figure 3.14: Distribution of turbulent kinetic energy in the radial direction

Like the velocity deficit, turbulent kinetic energy in the far wake field should follow a power law. There are several empirical relations proposed in the literature. The average value in our data in the far wake area suggests $k \sim d^{-0.33}$, which is very close to the theoretical value $d^{-1/3}$. However, the near wake results do not follow this relation.
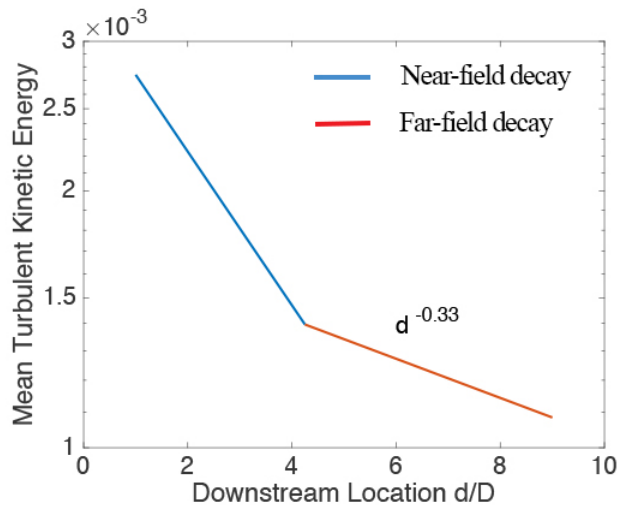
Figure 3.15: Decay of turbulent kinetic energy along the streamwise direction. The decay rate of the second section is close to the theoretical value –1/3.

To investigate the behavior of wake turbulence, it is necessary to identify the scales of flow structures. The following figure shows the spectra of the tested flows. Upstream the model, the flow is close to the ideal homogeneous turbulence. At 1D downstream, we can clearly see the elevation of spectrum line. At 10^2 m^{-1}, the red curve lifts up a little, indicating that there are lots of 0.5 to 1 cm structures in the flow. This is consistent with the size of the hub diameter. Further downstream, we find that the spectra at both 4.25D and 9D are close to the standard –5/3 slope line. No distinguishable peak can be identified.
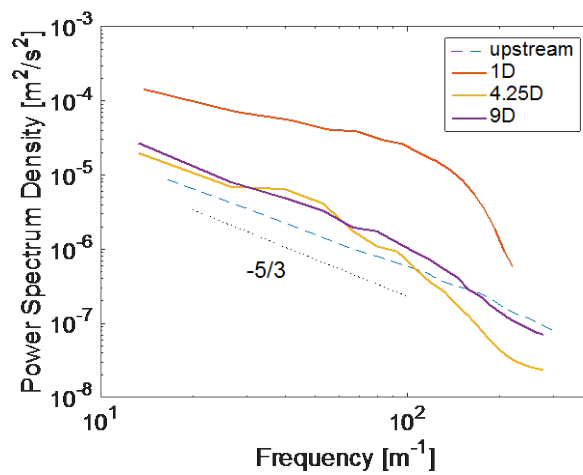
Figure 3.16: Spectra of turbulence up- and downstream the turbine model

3.2.3 Evolution of Vortex

To evaluate the decay of vortex in the flow, we used vorticity to identify the tip leakage vortex in the near wake. The following figure shows the vorticity contours and their boundaries by a contour line.
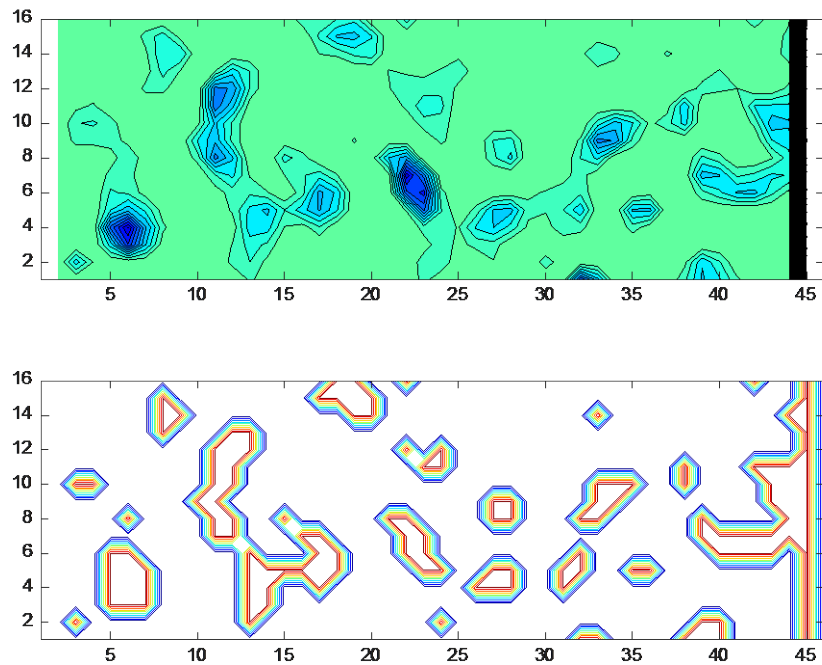
Figure 3.17: The upper figure is an instantaneous vorticity distribution in an arbitrary unit; the lower figure is the identified boundary of the vortices in the upper figure.

Integrating the vorticity in each identified vortex yields values for circulation, i.e., the strength of these vortices. The strength of the vortices decreases in the streamwise direction as shown in the following figures. From the normalized data, we can estimate the decrease rate to be about $\Gamma \sim d^{-0.2}$. This value is consistent with other experimental work $\Gamma \sim d^{-0.197}$.
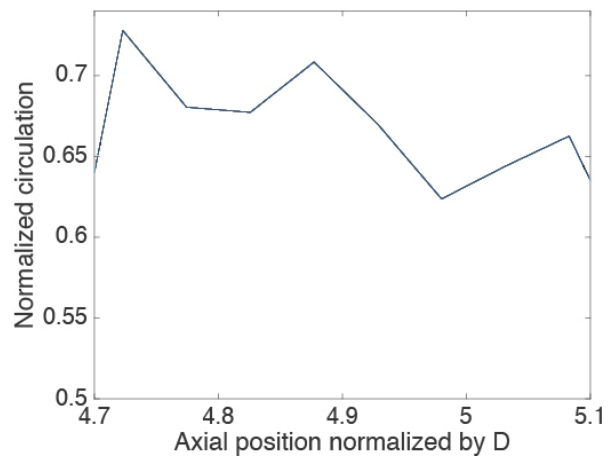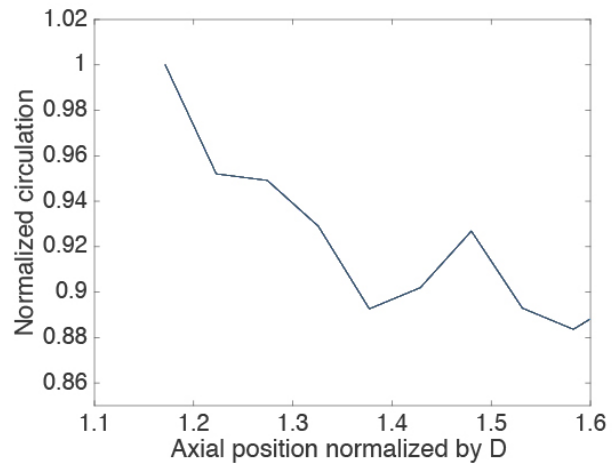
Figure 3.18: Decrease of vortex circulation in the streamwise direction

Chapter 4: Results and Discussion

In the first study (Mulinazzi & Zheng, 2014), two airports were used as case study sites due to airport projects and wind turbine proposals at the time. Their use in this study remains only to serve purposes of illustration. Parameters for wind turbines and aircraft are listed in Table 4.1.

Using the velocity field, the rolling moment coefficient acting on an airplane can be calculated. According to Equation 2.12, for a Cessna 172, the *hazard index* range for the wind turbine induced rolling moment coefficient is defined as: 1) High hazard: an induced rolling moment coefficient above 0.04; 2) Medium hazard: between 0.02 to 0.04; and 3) Low hazard: below 0.02.

**Table 4.1: Conditions of the wind turbine and the aircraft for the case study**

Center height (h)	Blade diameter (D)	Cessna 172 wingspan (L)	Wind speed range (v)
121.92 m	91.44 m	10.91 m	4.47 – 17.88 m/s

4.1 The Rooks County Case

Based on the calculated velocity distribution, the induced rolling momentum coefficient, and thus the roll *hazard index*, can be calculated near the runway from wind turbine wake to evaluate impact for the aircraft. We considered a possible condition of incoming wind speed to the wind turbine at 40 mph (17.88 m/s), which is assumed to be the highest possible safe wind speed under which wind turbines can operate. The circulation of the wind turbine wake helical vortex is $\Gamma = 116.89$ m^2/s (1258.19 ft^2/s) according to Equation 2.3. Using this circulation value, we simulated velocity field of a single turbine wake helical vortex. The resultant rolling moment and roll *hazard index* situation are shown in Figure 4.1. The rhombus area in Figure 4.1(a) is a cross section of the area where the helical vortex exists (between two orange lines) and the area near the runway from south to north (between the two green lines). Figure 4.1(a) shows the exact rolling moment value in the area and Figure 4.1(b) is the resultant *hazard index*. As shown in Figure 4.1(b), the area around the north portion of the runway is within the medium hazard region.
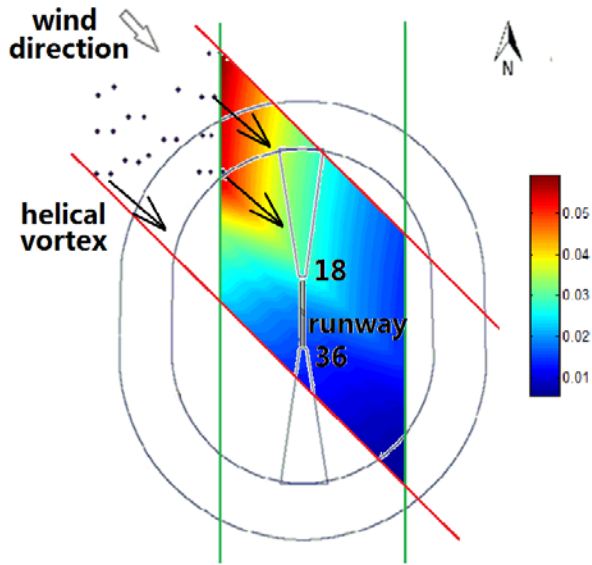
(a)
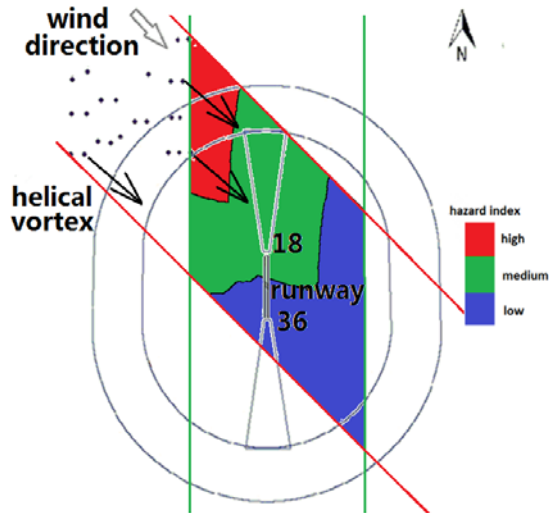
(b)

Figure 4.1: (a) Rolling moment coefficient, and (b) Roll *hazard index* around the Rooks County Airport

Figure 4.2 shows the vertical area of the roll *hazard index* above the runway. There are two approach surfaces: one is at a slope of 20:1, and the other at 34:1. The ground elevation is 1982 ft. The approach surface portion in the above plot is about 100 ft. Since the turbine tower center is 400 ft high, we extended the plot following the trend and put the contours of the rolling moment

coefficient in Figure 4.1 for the elevation between 2240 ft (the lowest blade tip elevation) and 2540 ft (the highest blade tip elevation). The zero in the distance in Figure 4.2 is at the north end of the runways, as indicated in Figure 4.1. The rolling moment coefficient along the runway, and the extended trend up to a distance of 10,660 ft (3250 m), is always in the high roll hazard range. But for the approach surfaces, only within the height between the two blade tips the airplane will experience a medium level of hazard.

Figure 4.2: Rolling moment distribution along the approach surface of Runway 18 (the colored region is all in the high roll *hazard index* range)

4.2 The Pratt Regional Airport Case

Based on the same velocity distribution calculation, the induced rolling momentum coefficient, and thus the roll *hazard index*, can be calculated from aircraft impact near the runway due to the wind turbine wake on the encountering aircraft. With the same assumption of highest possible safe wind at 17.88 m/s (40 mph), the circulation of the wind turbine wake helical vortex is $\Gamma = 116.89$ m^2/s (1258.19 ft^2/s) according to Equation 2.3. Using this circulation value, we simulated velocity field of a single turbine wake helical vortex. The resultant rolling moment and roll *hazard index* situation are shown in Figure 4.3. The rhombus area in Figure 4.3(a) is a cross section of the area where the helical vortex exists (between two orange lines) and the area near the runway from south to north (between the two green lines). Figure 4.3(a) shows the exact rolling

moment value in the area and Figure 4.3(b) is the resultant *hazard index*. As shown in Figure 4.3(b), the area around the runway is within the low hazard region.

(a)

(b)

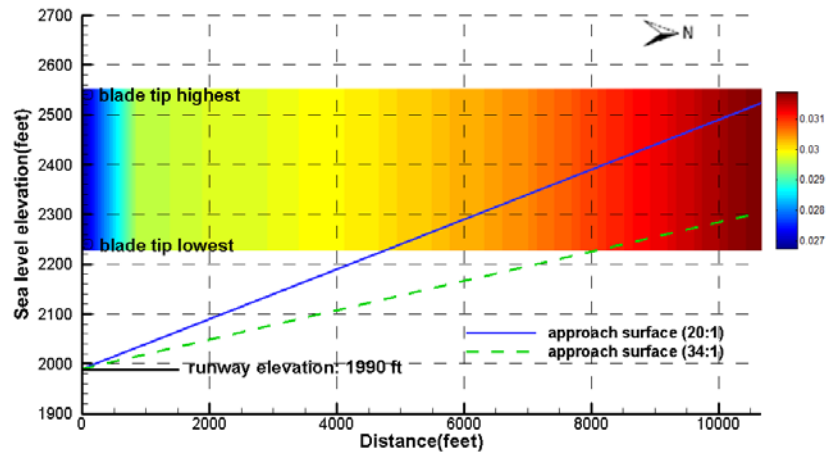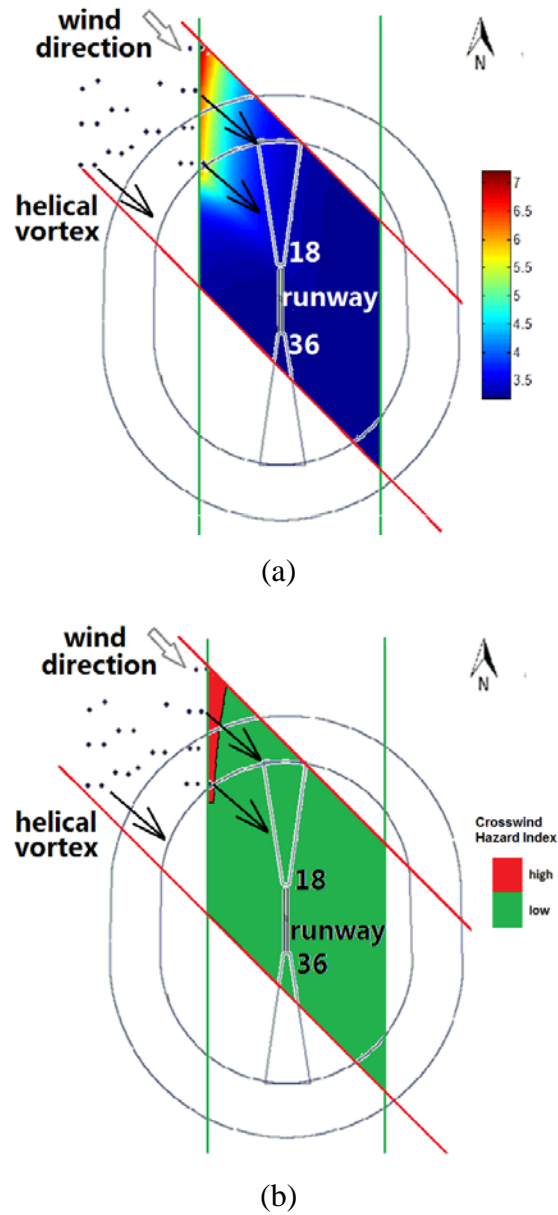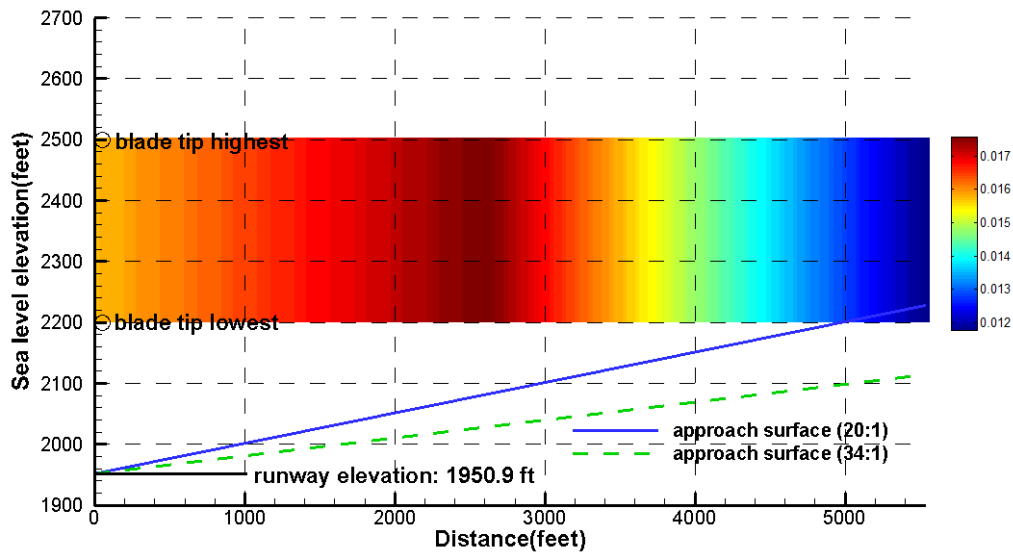**Figure 4.3: (a) Rolling moment coefficient, and (b) Roll *hazard index* around the Pratt Regional Airport**

Figure 4.4: Rolling moment distribution along the approach surface of Runway 18 (the colored region is all in the high roll *hazard index* range)

Figure 4.4 shows the vertical area of the roll *hazard index* above the runway just like Figure 4.2 in the Rooks County case. There are two approach surfaces: one is 20:1 approach surface and the other is 34:1 approach surface. The ground elevation is 1950.9 ft. Since the turbine tower center is 400 ft high, we extended the plot following the trend and put the contours of the rolling moment coefficient in Figure 4.4 for the elevation between 2200 ft (the lowest blade tip elevation) and 2500 ft (the highest blade tip elevation). Zero on the distance scale in Figure 4.4 is at the north end of the runways, as indicated in Figure 4.3. The rolling moment coefficient along this runway and the extended trend up to a distance of 5,540 ft (1689 m) is always in the high roll hazard range. But for the approach surfaces, the aircraft will encounter a low level of hazard within the height between the two blade tips of the approach surface at the slope of 20:1.

Chapter 5: Conclusions

A more accurate study has been conducted based upon the preliminary findings of our previous study (Mulinazzi & Zheng, 2014). The helical vortex model used for the wind turbine has been improved to remove the over-estimation of the velocity values near the center of the wind turbine vortex. The decay rate has been calibrated with an actuator-line method with the CFD calculation of the Navier–Stokes equations for fluid dynamics. The measurement, both in the wind tunnel and water tunnel, has been carried out for comparison with the theoretical models. Case studies for the airports in Rooks County and Pratt are used to implement the prediction model. The roll *hazard indices* for these two airports are calculated for the particular wind turbines and a GA aircraft, the Cessna 172. These examples have shown that the models developed from theoretical practicality can be validated at different locations. Furthermore, they yield values for the *hazard index* developed from the initial study (Mulinazzi & Zheng, 2014) that are useful to assess the potential or likely impacts from small GA aircraft from wind turbine wake turbulence. Conceivably, the *hazard index* could be applied to evaluate wind turbine sites in proximity to airports. Extending use of the *hazard index* to other airports or other aircraft types must account for local conditions in prevailing winds, aircraft/airfoil tolerance for turbulent conditions, assumptions for aircraft approach speeds, and any adjustments for examining different approach slopes. The worst scenario that could be derived from the *hazard index*, when applied to given conditions in relation to a wind farm proposal near a GA airport, can be considered a "safety check" against proposed wind turbine sites.

The study of wind turbines and how the turbulences that they produce affect general aviation aircraft need further study. The theoretical models that were produced in this report should be modified and enhanced with future studies that could include measurements using UAVs and lidars.

References

Fukumoto, Y., & Okulov, V. L. (2005). The velocity field induced by a helical vortex tube. *Physics of Fluids, 17*(10), 107101.

Goode, M. W., O'Bryan, T. C., Yenni, K. R., Cannaday, R. L., & Mayo, M. H. (1976). *Landing practices of general aviation pilots in single-engine light airplanes* (NASA TN D-8283). Washington, DC: National Aeronautics and Space Administration.

Hardin, J. C. (1982). The velocity field induced by a helical vortex filament. *Physics of Fluids, 25*(11), 1949-1952.

Jin, W. (2013). *Numerical simulation of wind turbine wakes based on actuator line method in NEK5000* (Master's thesis). KTH Royal Institute of Technology, Stockholm, Sweden.

Mulinazzi, T. E., & Zheng, Z. C. (2014). *Wind farm turbulence impacts on general aviation airports in Kansas* (K-TRAN: KU-13-6). Topeka, KS: Kansas Department of Transportation.

O'Dea, M. L. & Guessous, L. (2016). Further developments in numerical simulations of wind turbine flows using the actuator line method. In *Proceedings of the ASME 2016 Fluids Engineering Division Summer Meeting*.

Peet, Y., Fischer, P., Conzelmann, G., & Kotamarthi, V. (2013). Actuator line aerodynamics model with spectral elements. In *51st IAA Aerospace Sciences Meeting including the New Horizons Forum and Aerospace Exposition*.

Roskam, J. (1979). Appendix C: Summary of Laplace transform properties. In *Airplane flight dynamics and automatic flight controls, Part I*. Lawrence, KS: Roskam Aviation and Engineering Corporation.

Sadraey, M. H. (2012). *Aircraft design: A systems engineering approach*. Hoboken, NJ: Wiley.

Sarpkaya, T., Robins, R. E., & Delisi, D. P. (2001). Wake-vortex eddy-dissipation model predictions compared with observations. *Journal of Aircraft, 38*(4), 687–692.

Sherry, M., Sheridan, J., & Lo Jacono, D. (2013). Characterisation of a horizontal axis wind turbine's tip and root vortices. *Experiment in Fluids, 54*(3), 1417.

Troldborg, N. (2009). *Actuator line modeling of wind turbine wakes* (Doctoral dissertation). Technical University of Denmark, Lyngby, Denmark.

Zhang, N., & Zheng, Z. C. (2007). An improved direct-forcing immersed-boundary method for finite difference applications. *Journal of Computational Physics, 221*(1), 250–268.

Zheng, Z. C., & Xu, Y. (2008). A visualized wake hazard assessment (Paper # AIAA 2008-467). *46th AIAA Aerospace Sciences Meeting and Exhibit*, January 7-10, 2008, Reno, Nevada.

Zheng, Z. C., Xu, Y., & Wilson, D. K. (2009). Behaviors of vortex wake in random atmospheric turbulence. *Journal of Aircraft, 46*(6), 2139–2144.

K-TRAN

KANSAS TRANSPORTATION RESEARCH
AND
NEW-DEVELOPMENT PROGRAM

AD ASTRA PER ASPERA

Kansas
Department of Transportation